Chemistry–A European Journal

Supporting Information

Coexistence of Spin–Lattice Relaxation and Phonon-Bottleneck Processes in Gd^{III}–Phthlocyaninato Triple-Decker Complexes under Highly Diluted Conditions

Yoji Horii,*[a] Keiichi Katoh,*[b] Yuji Miyazaki,[c] Marko Damjanović,[d] Tetsu Sato,[b] Liviu Ungur,[e] Liviu F. Chibotaru,[f] Brian K. Breedlove,[b] Motohiro Nakano,[c] Wolfgang Wernsdorfer,[d] and Masahiro Yamashita*[a, b, g]

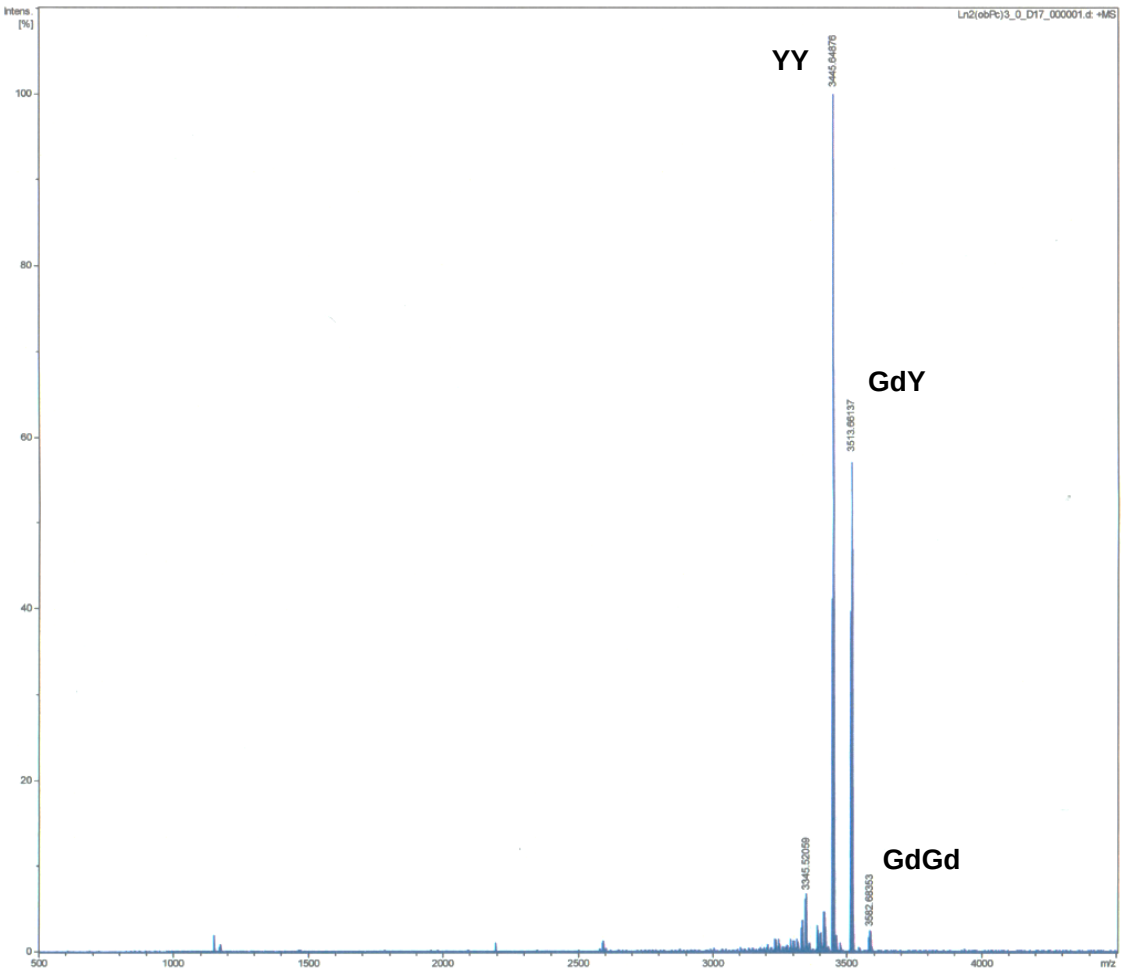

Figure S1. ESI-MS spectrum of GdY sample. The ratio of peak areas of **YY**, **GdY** and **GdGd** is 49:49:2, which correspond to Gd:Y = 27:73.

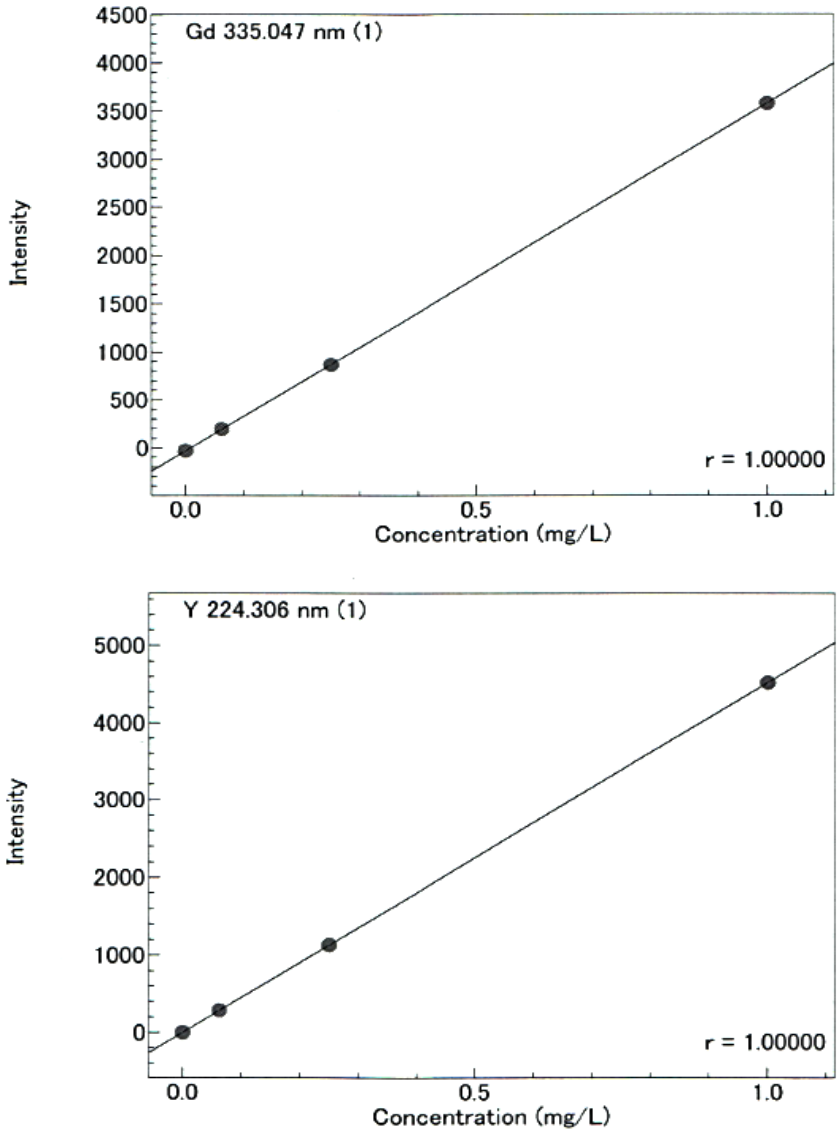

Figure S2. ICP-AES calibration curves for Gd and Y.

Table S1. Concentration and molar ratio of Gd and Y in the GdY sample.

	Gd	Y
Wavelength/nm	335.047 (1)	224.306 (1)
Concentration/ppm	0.259	0.277
Molar ratio	34.6%	65.4%

Table S2. Crystal parameters for GdGd and GdY.

	GdGd	GdY
Formula	$C_{98}H_{126}GdN_{12}O_{13}$	$C_{98}H_{126}Gd_{0.33}N_{12}O_{13}Y_{0.66}$
Crystal system	triclinic	triclinic
Space group	*P*–1	*P*–1
a/Å	13.203(3)	13.1502(2)
b/Å	17.882(4)	17.8665(3)
c/Å	20.750(4)	20.6774(4)
α/°	107.439(2)	107.371(2)
β/°	90.415(3)	90.463(2)
γ/°	100.850(3)	100.8360(10)
V/Å^3	4579.7(17)	4543.17(14)
Z	2	2
T/K	100	100
ρ_{calcd}/ g cm^{-3}	1.332	1.310
R_1	0.0417	0.0372
wR_2	0.1005	0.0971
GOF	1.068	1.045

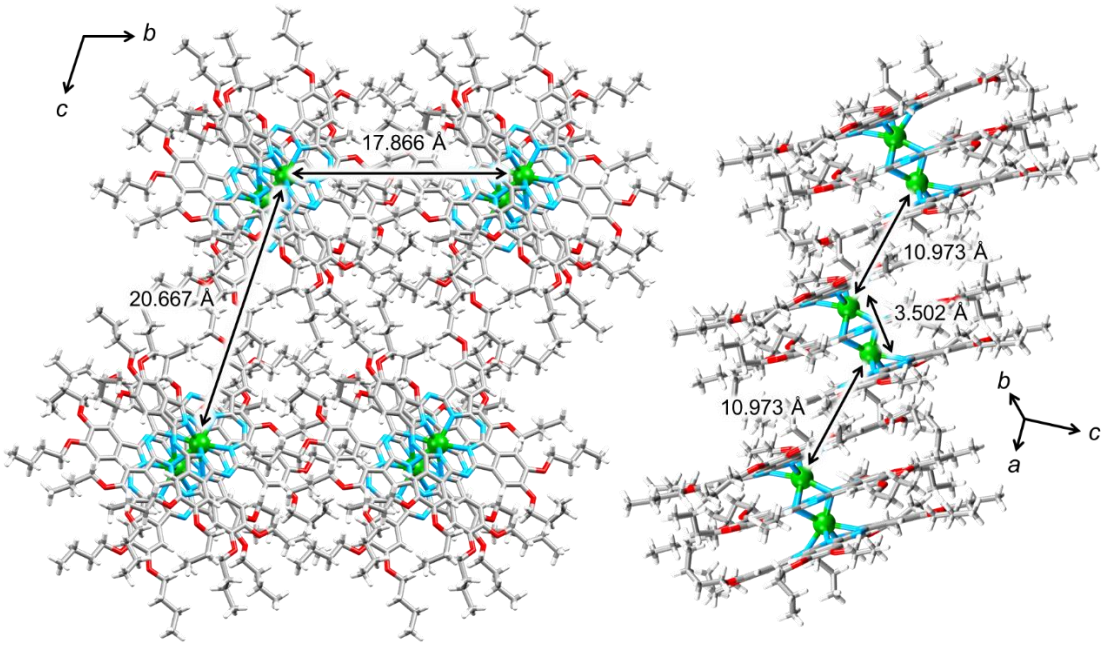

Figure S3. Packing structures and metal–metal distances of **GdY**. Gd:Y = 0.37:0.67. Color scheme: green, Gd; gray, C; red, O; blue, N.

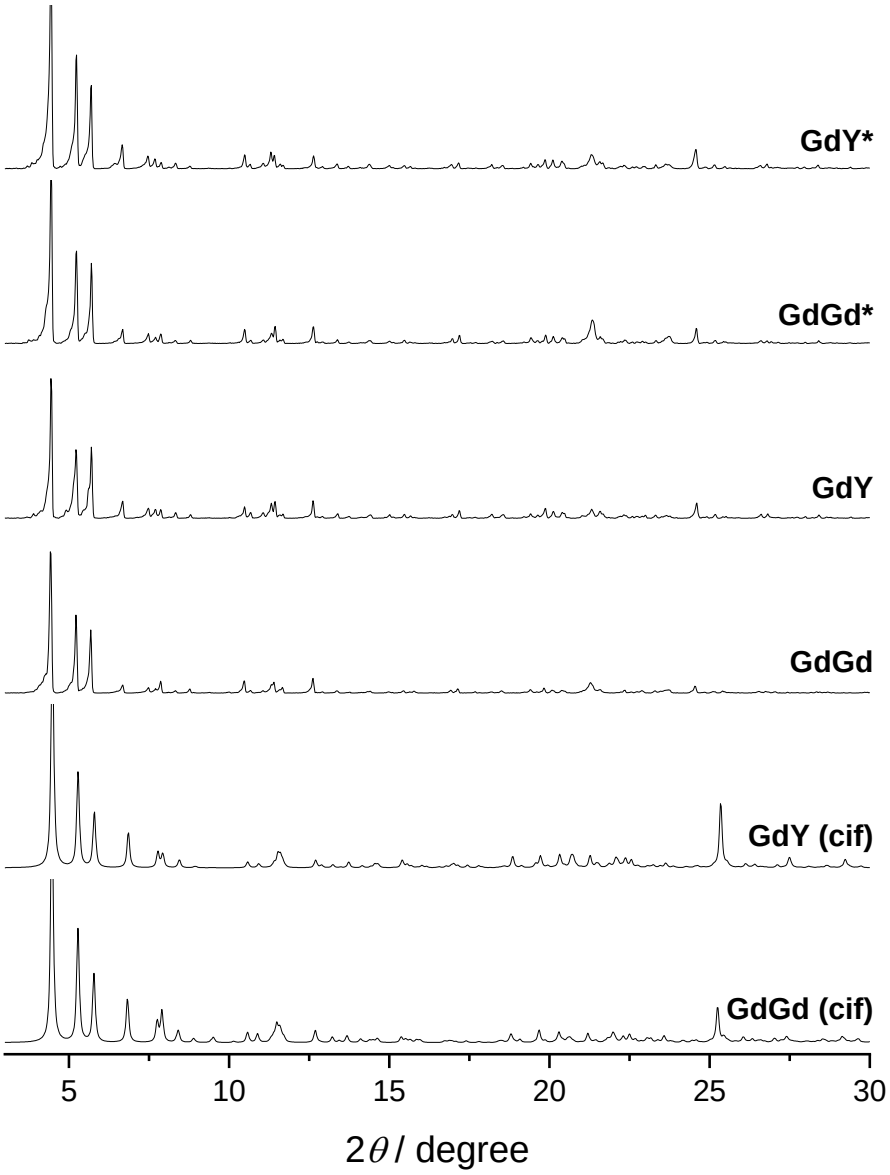

Figure S4. Powder X-ray diffraction patterns for triple-decker complexes. **GdGd** (cif) and **GdY** (cif) are patterns simulated using cif files.

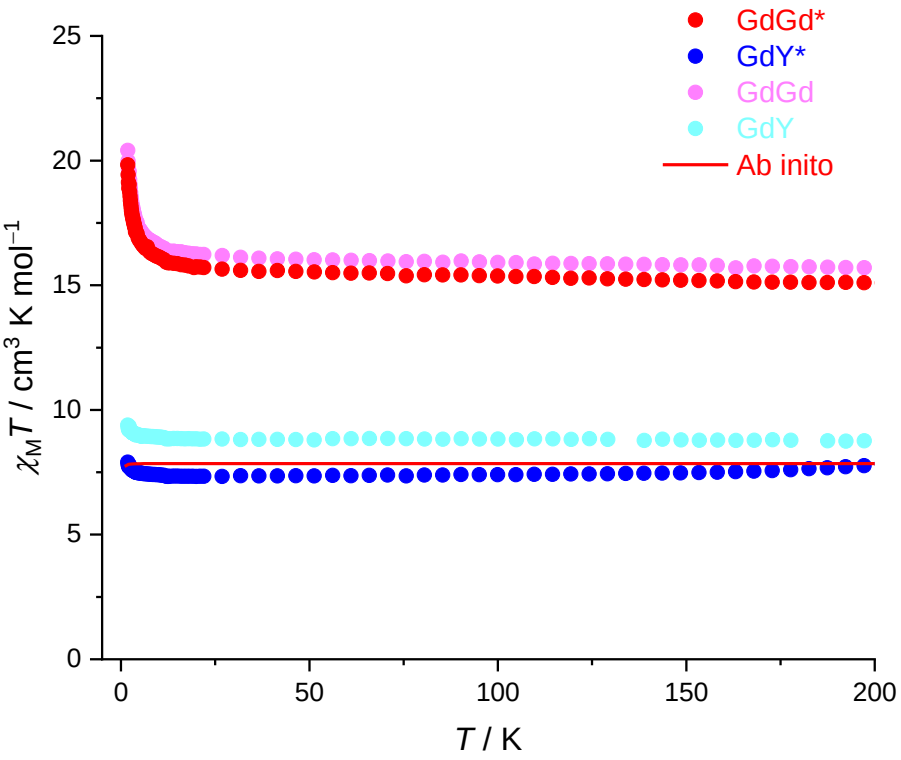

Figure S5. $\chi_M T$ vs T plots for magnetically diluted samples (**GdGd*** and **GdY***). The $\chi_M T$ values for undiluted samples are slightly larger than those in diluted samples over the entire T range possibly because of the experimental error of mixing samples. However, the both plots are similar with each other, indicating the negligible magnitude of intramolecular magnetic interactions. Details of the ab initio calculation were shown in the next section.

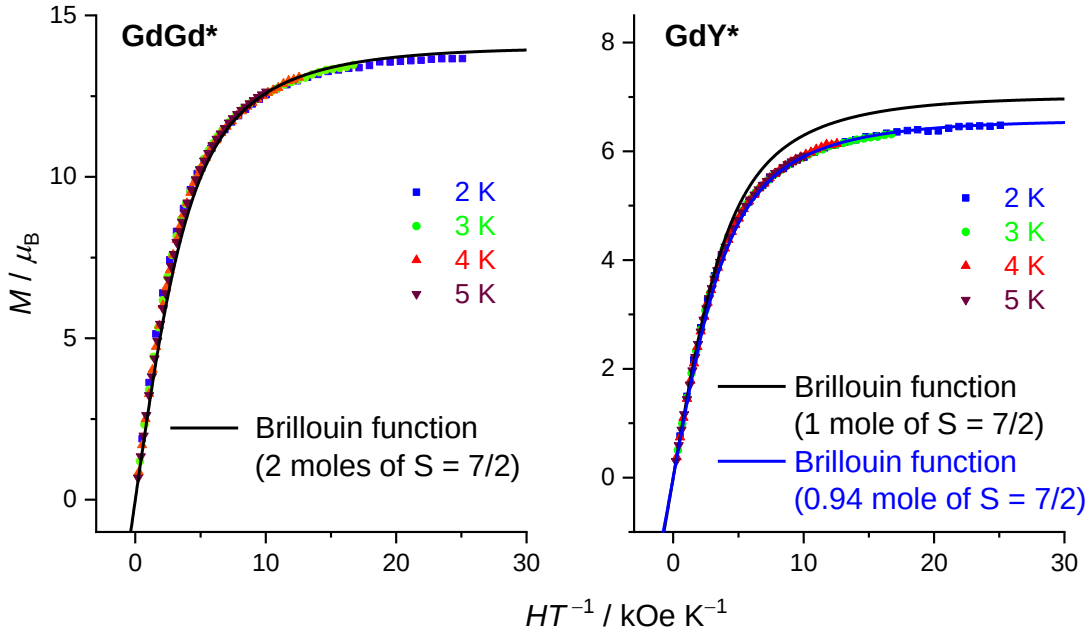

Figure S6. *M* vs HT^{-1} plot for **GdGd*** and **GdY***. *T*-independent behaviour and agreement with the Brillouin functions (solid curves) indicate the absence of significant magnetic anisotropy on Gd(III) ions.

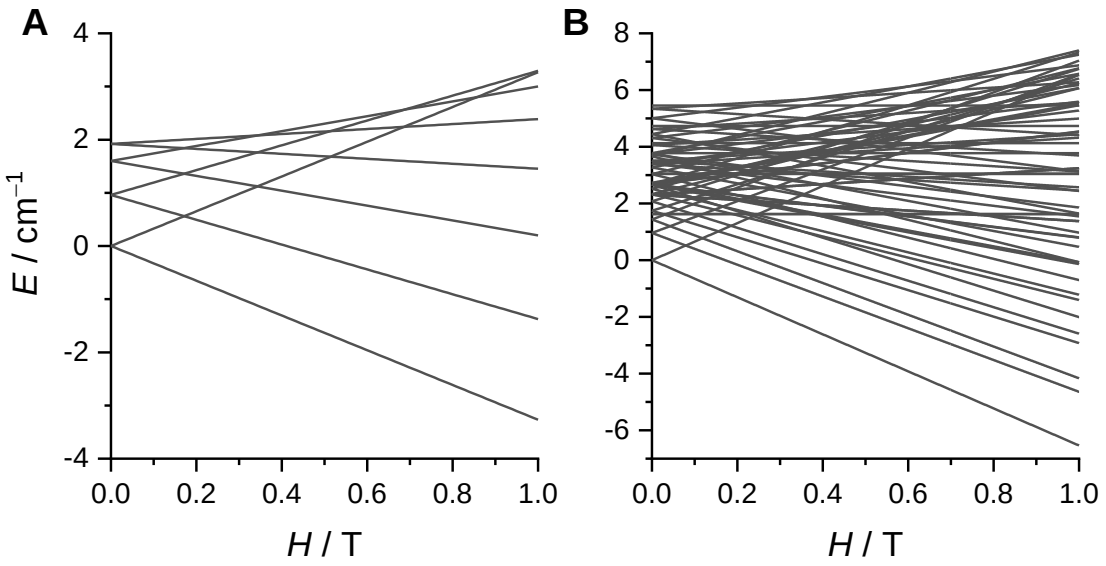

Figure S7. Zeeman diagrams for (A) **GdGd*** and (B) **GdY***. ZFS parameters obtained form the magnetic measurements and the heat capacity measurements (D = −0.160 cm^{-1}) was applied to the Gd^{3+} ions. Exchange interactions between Gd^{3+}-Gd^{3+} (J_{ex} = 0.0340 cm^{-1}) was applied for **GdGd**.

Ab Initio calculations on Gd(III) site

Ab initio calculations were conducted using the CASSCF/RASSI/SINGLE_ANISO modules in MOLCAS version 8.2 program.[1-2]

The structural model for ab initio calculations was made by modifying the crystal structure of **GdGd**, where *n*-buotxy chains and the opposite one side of the ligands were omitted and one Gd(III) ion was replaced with a diamagnetic Y(III) ion.

Table S3. Basis sets used for ab initio calculations.

Atom	Basis set
Gd	ANO-RCC-VDZP
Y N C H	ANO-RCC-VDZ

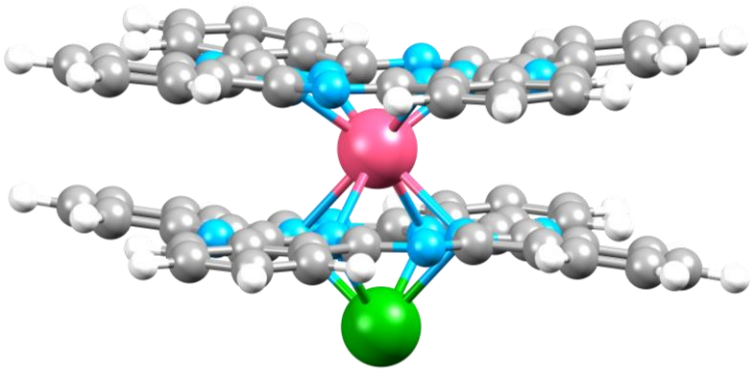

Figure S8. Structural model for ab initio calculations. The *n*-butoxy chains of **GdGd** were replaced with H atoms, and the opposite side of the obPc ligand and Gd(III) ion were omitted and replaced with Y(III), respectively. Color scheme: pink, Gd; green, Y; gray, C; blue, N; white, H.

Table S4. Ab initio zero-field splitting energy for Gd(III) site.

Wave functions	*Energy* / cm^{-1}	Main values of *g* tensor considering the *S* = 1/2 spin
|±7/2>	0.000	g_x = 0.002669304 g_y = 0.002881414 g_z = 13.971608723
0.82|±5/2>+0.58|∓5/2>	0.621	g_x = 0.205366841 g_y = 0.210396807 g_z = 9.967731222
0.77|±3/2>+0.63|∓3/2> +0.09|∓1/2>+0.08|±1/2>	1.015	g_x = 1.678372971 g_y = 1.972525345 g_z = 5.872271427
0.91|±1/2>+0.40∓|1/2> +0.11|∓3/2>+0.04|±3/2>	1.214	g_x = 9.747704907 g_y = 6.086961469 g_z = 1.891402373

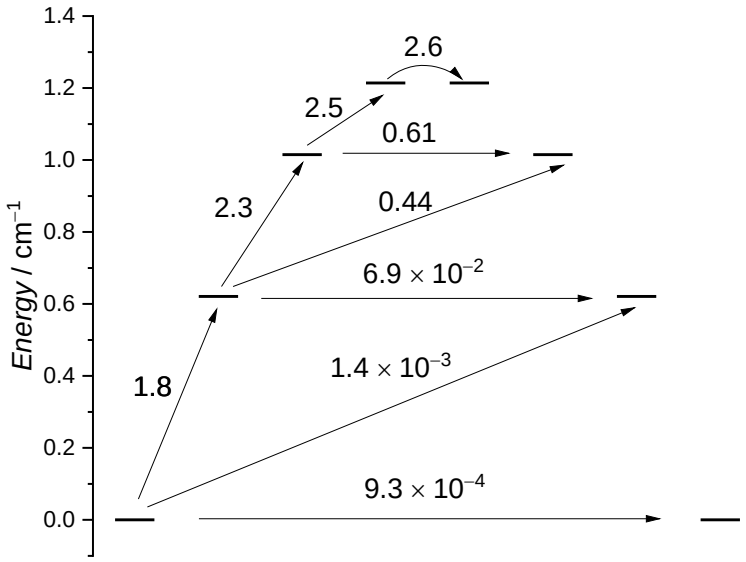

Figure S9. Zero-field splitting energy for a Gd(III) ion. The arrows and the numbers indicate the relaxation pathways estimated from the matrix elements of magnetic momentum μ = (μ_x, μ_y, μ_z) connecting eigenstates.[3]

Determination of lattice heat capacity

Lattice heat capacities below 20 K were determined using the following equation:

$$C_p = E_1 T^{-2} + C_3 T^3 + C_5 T^5 + C_7 T^7 + C_9 T^9 \qquad \text{Eq. S1}$$

where the first term is the high temperature side of the Schottky contribution, and the latter terms represent the lattice contributions. Fitting (dotted curve in Figure S9A) using the C_p of **GdGd** in the T range of 2.7–20 K in a zero dc field gave the parameters summarized in Table S5. Removing the ET^{-2} term from the fitted curve affords C_{lat} (solid curve in Figures S9A and B). The C_{lat} overlaps with the C_p of diamagnetic **YY** in a zero dc field and **GdGd** at 9 T, supporting that the derived C_{lat} is reliable.

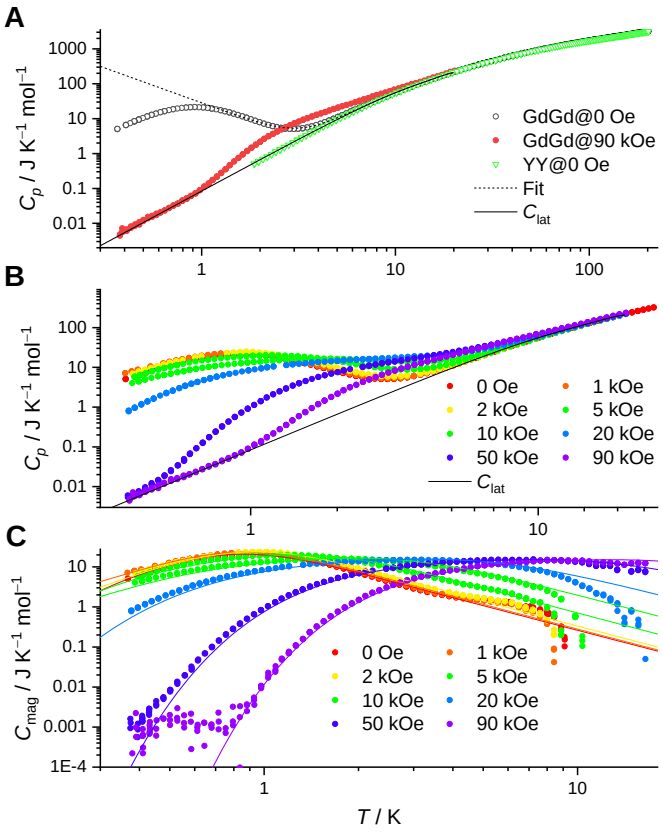

Figure S10. (A) Determination of the lattice heat capacities (C_{lat}) below 20 K. (B) DC magnetic field dependences of C_p for **GdGd**. (C) C_{mag} of **GdGd**. Solid curves were fitted using the PHI program.

Table S5. Optimized parameters using Eq. S1.

E_1	C_3	C_5	C_7	C_9
28.3	8.44×10^{-2}	-3.79×10^{-4}	9.96×10^{-7}	-1.03×10^{-7}

Extended Debye model equations

Since the ac magnetic susceptibilities of the present samples sometimes show dual magnetic relaxations, these were simulated by using the extended Debye model equations, in which two Debye's equations with dispersion coefficient were combined.

$$\chi'_{\mathrm{M}} = \chi_{\mathrm{S}} + (\chi_{\mathrm{T}} - \chi_{\mathrm{S}}) \left[\frac{\beta \left\{ 1 + (2\pi\nu\tau_1)^{1-\alpha_1} \sin\left(\frac{1}{2\pi\alpha_1}\right) \right\}}{1 + 2(2\pi\nu\tau_1)^{1-\alpha_1} \sin\left(\frac{1}{2\pi\alpha_1}\right) + (2\pi\tau_1)^{2-2\alpha_1}} + \frac{(1-\beta) \left\{ 1 + (2\pi\nu\tau_2)^{1-\alpha_2} \sin\left(\frac{1}{2\pi\alpha_2}\right) \right\}}{1 + 2(2\pi\nu\tau_2)^{1-\alpha_2} \sin\left(\frac{1}{2\pi\alpha_2}\right) + (2\pi\tau_2)^{2-2\alpha_2}} \right] \quad \text{Eq. S1a}$$

$$\chi''_{\mathrm{M}} = (\chi_{\mathrm{T}} - \chi_{\mathrm{S}}) \left[\frac{\beta (2\pi\nu\tau_1)^{1-\alpha_1} \cos\left(\frac{1}{2\pi\alpha_1}\right)}{1 + 2(2\pi\nu\tau_1)^{1-\alpha_1} \sin\left(\frac{1}{2\pi\alpha_1}\right) + (2\pi\tau_1)^{2-2\alpha_1}} + \frac{(1-\beta)\beta (2\pi\nu\tau_2)^{1-\alpha_2} \cos\left(\frac{1}{2\pi\alpha_2}\right)}{1 + 2(2\pi\nu\tau_2)^{1-\alpha_2} \sin\left(\frac{1}{2\pi\alpha_2}\right) + (2\pi\tau_2)^{2-2\alpha_2}} \right] \quad \text{Eq. S1b}$$

In these equations, χ_{S} is adiabatic susceptibility, χ_{T} is isothermal susceptibility, τ_1 and τ_2 are relaxation times, α_1 and α_2 are dispersion factor, β is the ratio of two relaxations.

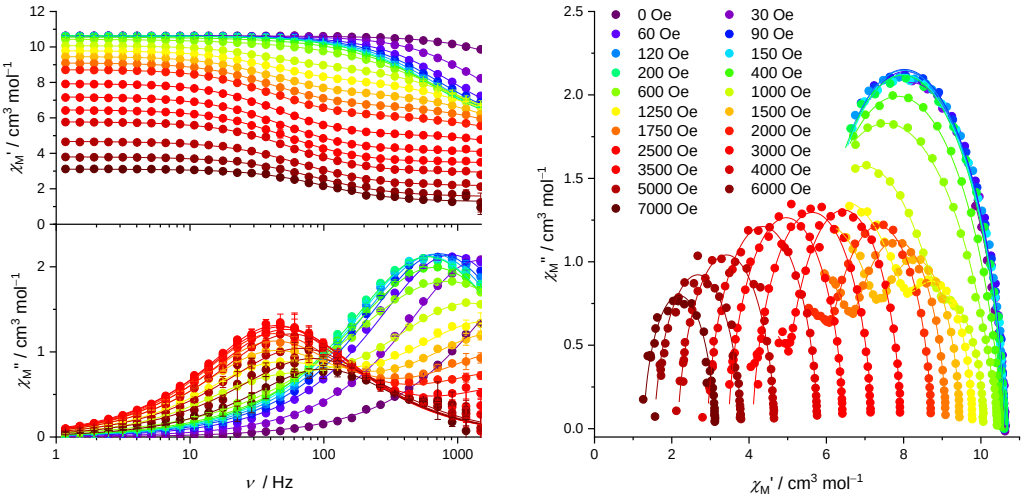

Figure S11. DC field dependences of the ac magnetic susceptibilities of **GdGd*** at 1.85 K. Solid curves represent fit using Debye model.

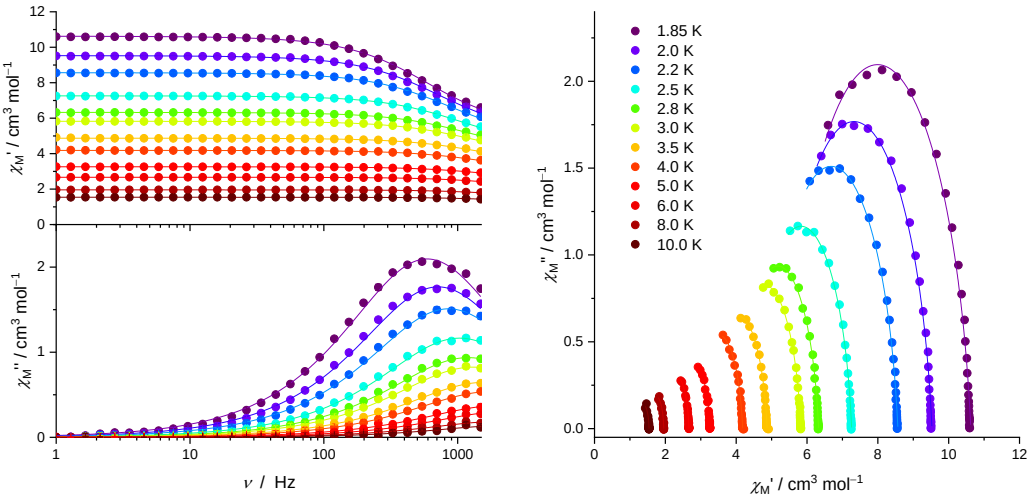

Figure S12. Temperature dependences of the ac magnetic susceptibilities of **GdGd*** in a field of 200 Oe. In this dc field, FR was observed. Solid curves represent fit using Debye model.

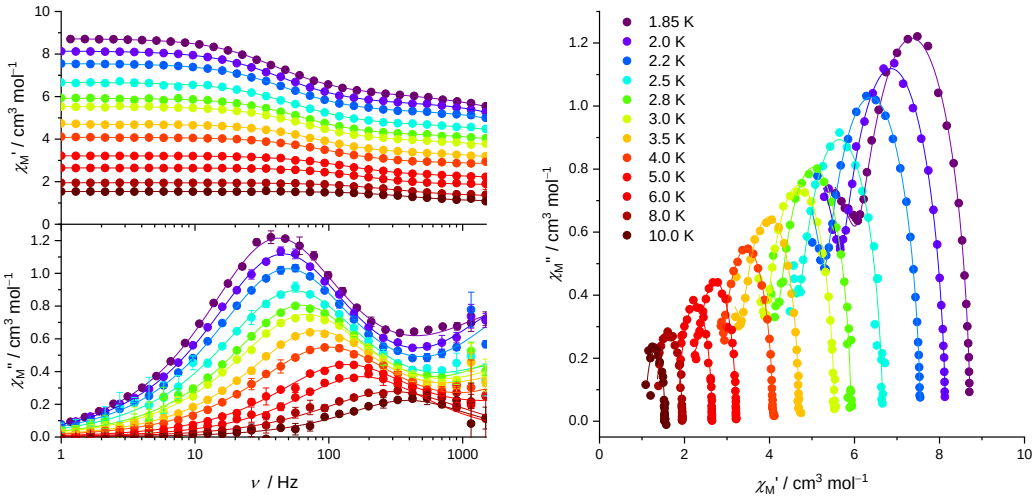

Figure S13. Temperature dependences of the ac magnetic susceptibilities of **GdGd*** in a field of 2 kOe. At this dc field strength, SR was observed. Solid curves represent fit using Debye model.

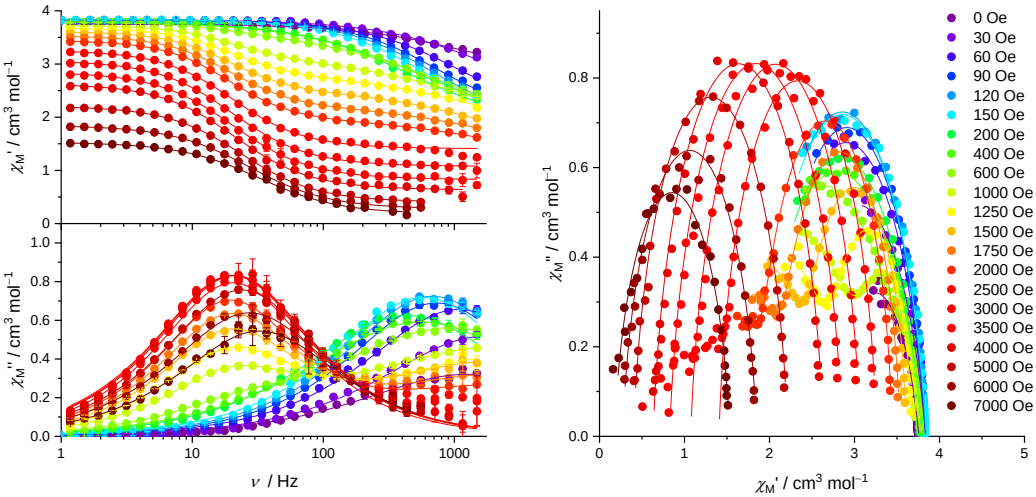

Figure S14. DC field dependences of the ac magnetic susceptibilities of **GdY*** at 1.85 K. Solid curves represent fit using Debye model.

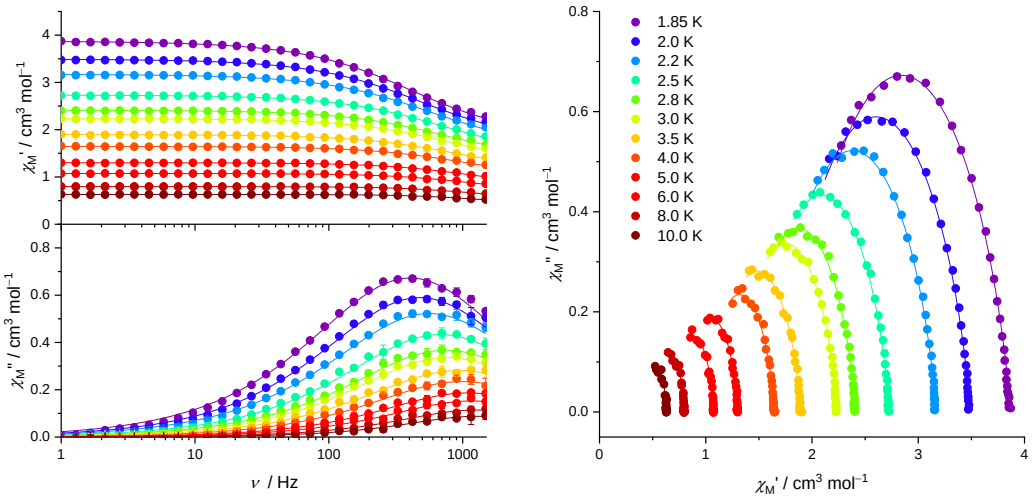

Figure S15. Temperature dependences of the ac magnetic susceptibilities of **GdY*** in a field of 200 Oe. At this dc field strength, FR was observed. Solid curves represent fit using Debye model.

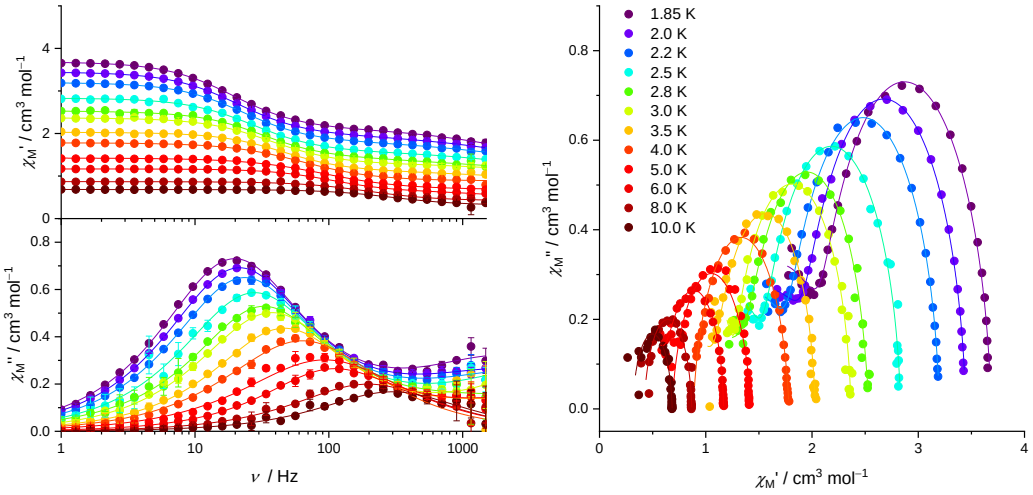

Figure S16. Temperature dependences of the ac magnetic susceptibilities of **GdY*** in a field of 2 kOe. At this dc field strength, SR was observed. Solid curves represent fit using Debye model.

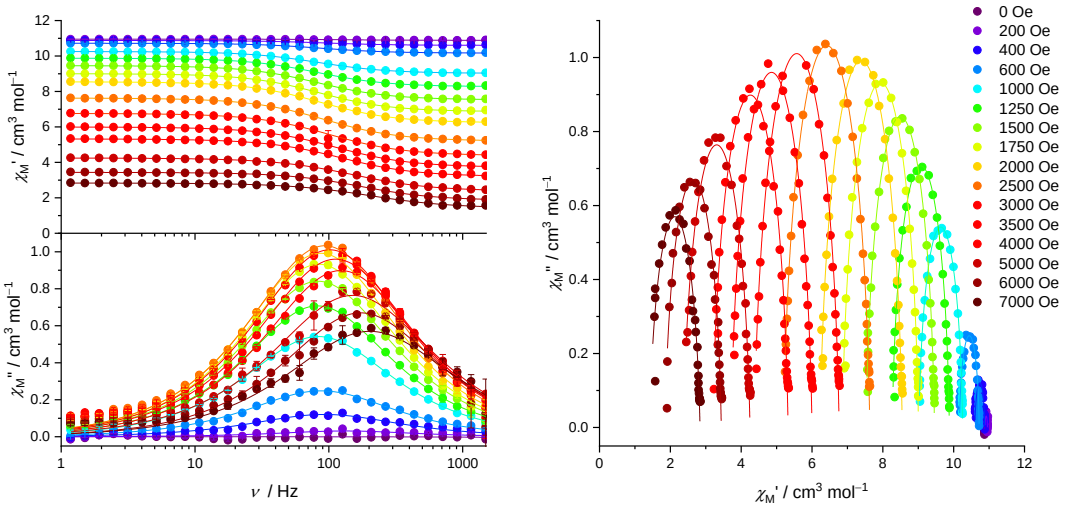

Figure S17. DC field dependences of the ac magnetic susceptibilities of **GdGd** at 1.85 K. Solid curves represent fit using Debye model.

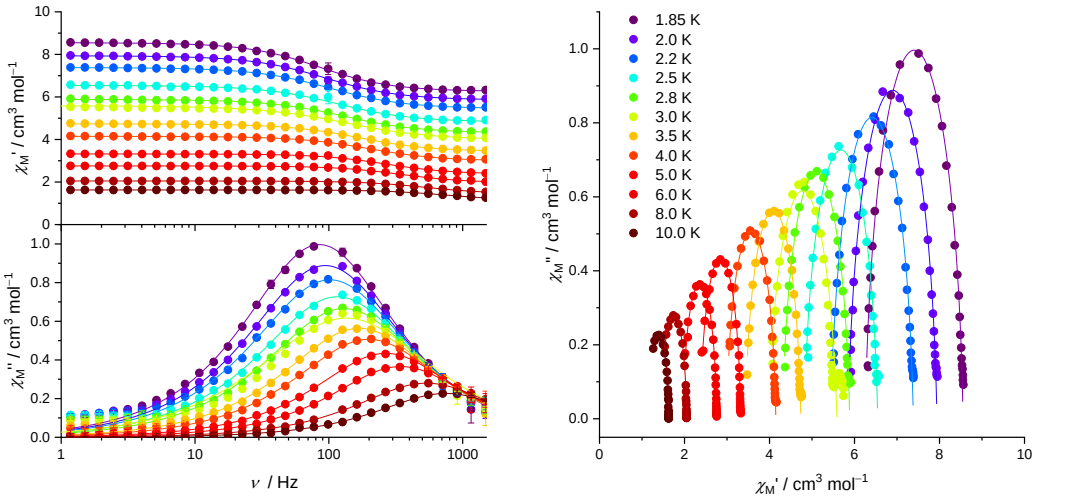

Figure S18. Temperature dependences of the ac magnetic susceptibilities of **GdGd** in a field of 2 kOe. At this dc field strength, SR was observed. Solid curves represent fit using Debye model.

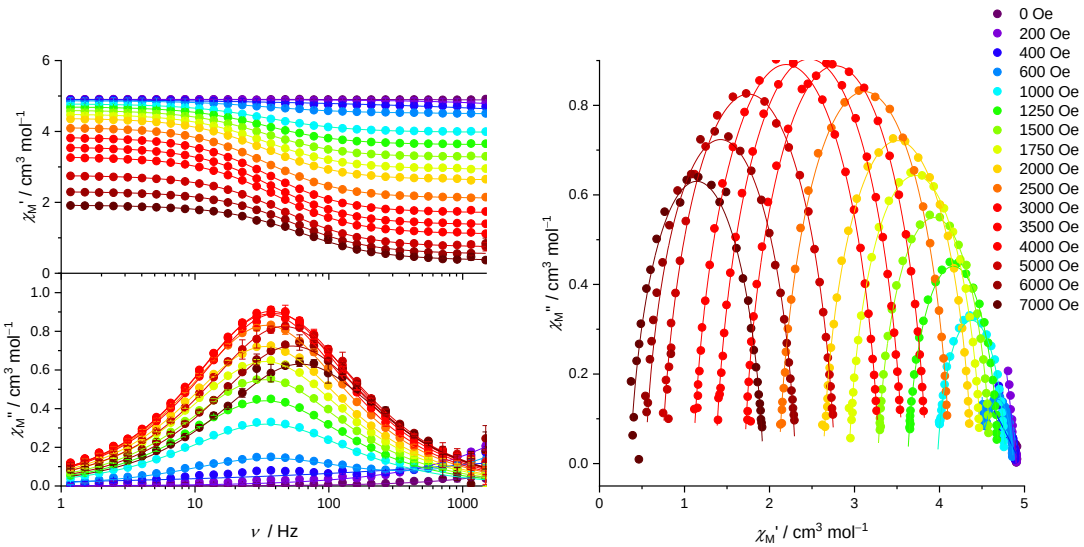

Figure S19. DC field dependences of the ac magnetic susceptibilities of **GdY** at 1.85 K. Solid curves represent fit using Debye model.

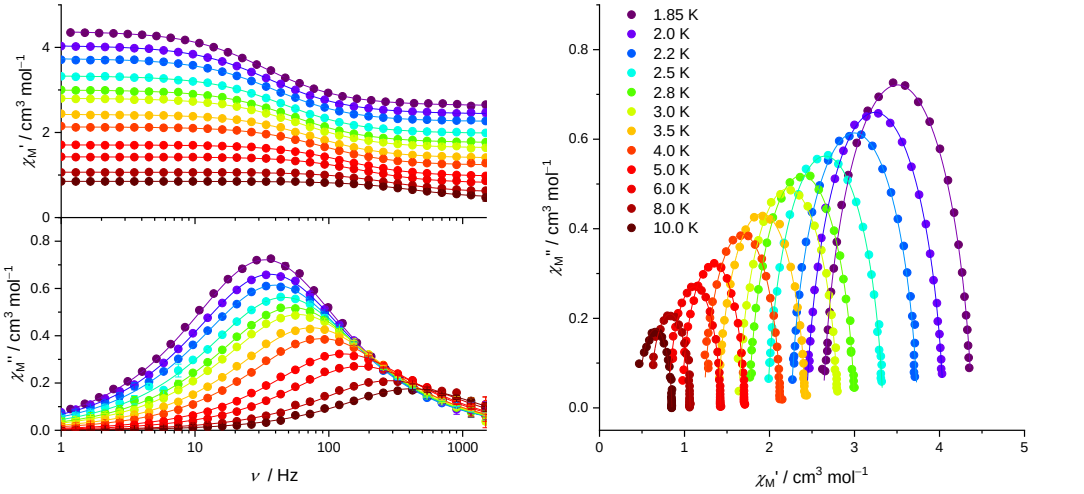

Figure S20. Temperature dependences of the ac magnetic susceptibilities of **GdY** in a field of 2 kOe. At this dc field strength, SR was observed. Solid curves represent fit using Debye model.

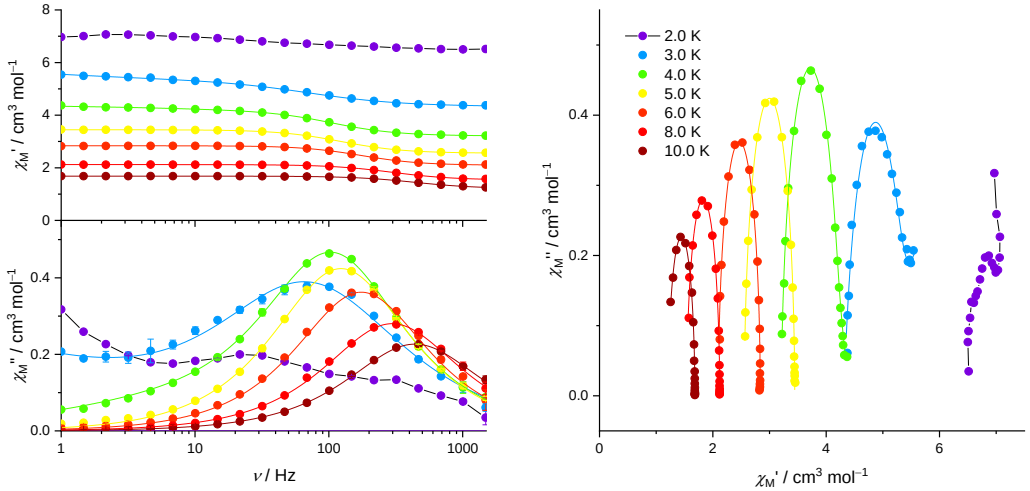

Figure S21. Temperature dependences of the ac magnetic susceptibilities of pristine crystals **GdGd$_c$** in a field of 2 kOe. The crystals were loaded into NMR tubes with their mother liquor, degassed by using freeze pump thaw processes, and then the tubes were flame sealed to avoid the loss of crystal solvent. In this dc field, SR was observed. Solid curves except 2 K represent fit using Debye model.

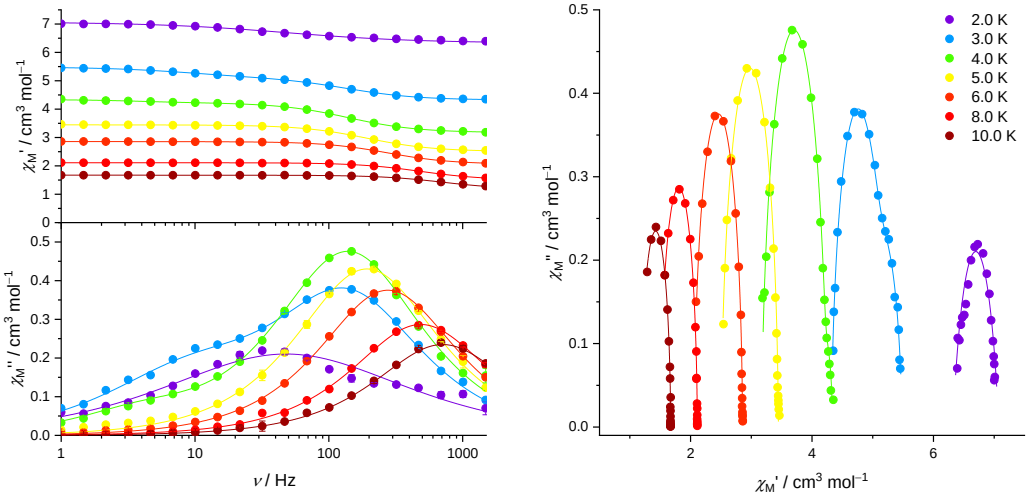

Figure S22. Temperature dependences of the ac magnetic susceptibilities of crushed **GdGd$_c$** in a field of 2 kOe. After acquiring the data shown in Figure S20, the NMR tube was opened, and the crystals were crushed using a spatula. Then the tubes were flame sealed again after a few freeze pump thaw processes. The curves below 3 K were affected by crushing the crystals.

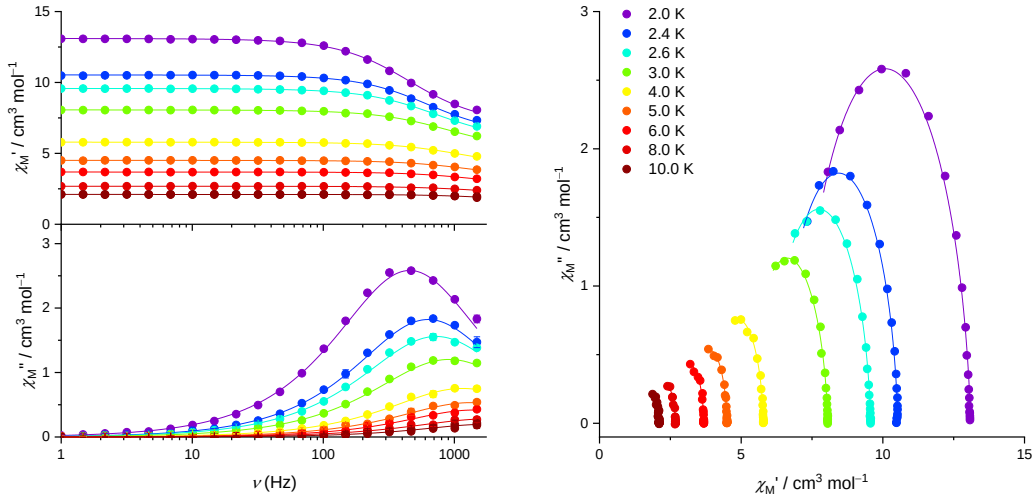

Figure S23. Temperature dependences of the ac magnetic susceptibilities of pristine crystals **GdGd$_c$*** in a 200 Oe field. Crystals were loaded into NMR tube with their mother liquor, which was degassed by freeze pump thaw processes, and then the tubes were flame sealed to avoid the loss of crystal solvent. In this dc field, FR was observed. Solid curves represent fit using Debye model.

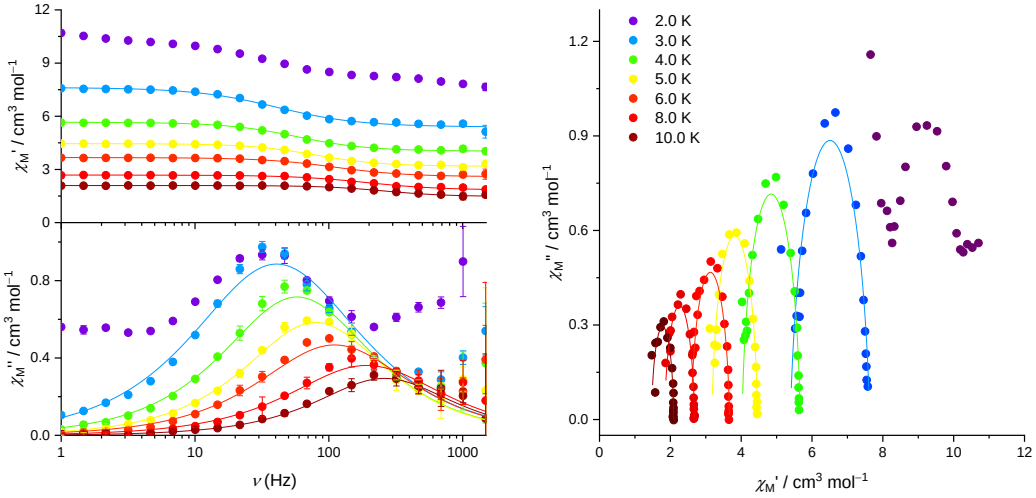

Figure S24. Temperature dependences of the ac magnetic susceptibilities of pristine crystals **GdGd$_c$*** at 2 kOe. Solid curves except 2 K represent fit using Debye model.

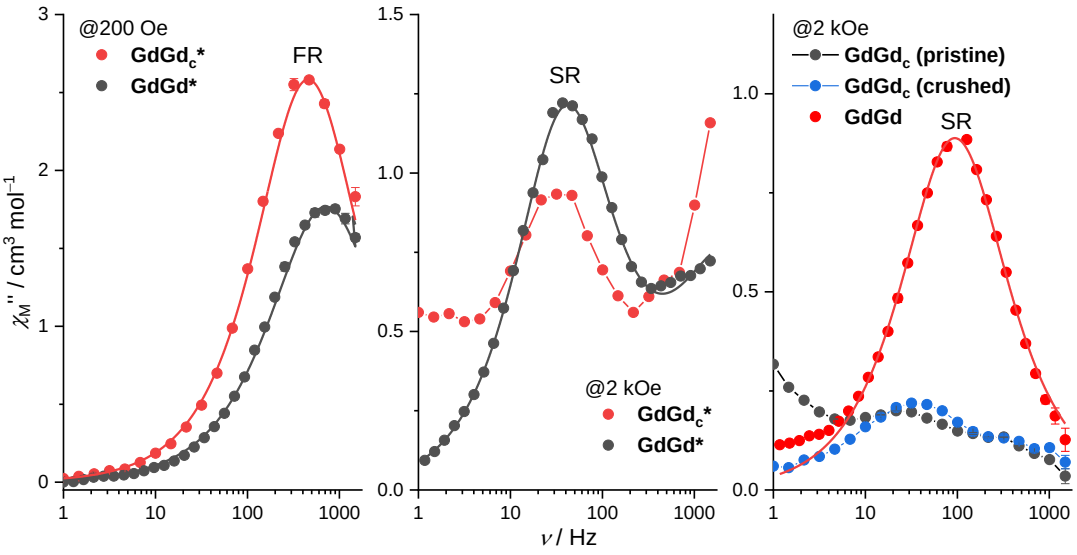

Figure S25. Crystalline size dependence of FR and SR. The shapes of cM'' vs n plots of SR changed by crushing the crystal, indicating the contribution of PB.

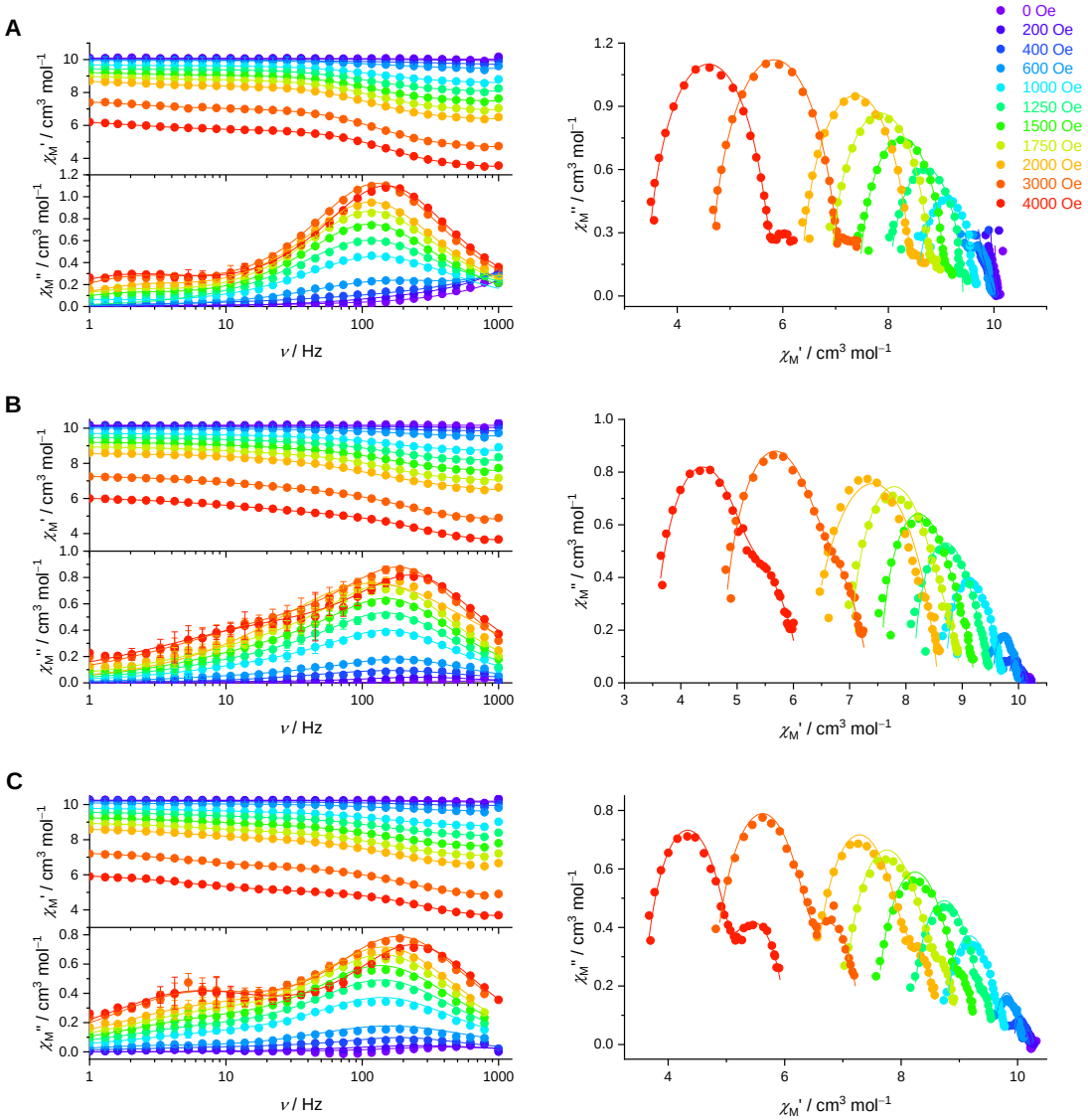

Figure S26. AC magnetic susceptibilities of diluted samples containing (A) 25 mol% (B) 50 mol% and (C) 75 mol% **GdGd** at 2 K. The small tail of the χ_M'' peaks attributed to SR starts to be observed in fields of 0 and 200 Oe for 25 mol% sample. Clear ac peaks of SR appear at 100 Hz in a field of >1000 Oe dc field. Due to the crystal size effects, the small peaks were observed below 10 Hz.

Simulation of dual magnetic relaxations

Although fitting the ac magnetic susceptibilities using Eq. S1 was performed to obtain τ_1 and τ_2, there is no theoretical meaning to it. The model of ac magnetic susceptibilities accounting for heat transport among spin system, lattice and thermal bath, as shown in Figure S25, is expressed below.[4-5]

$$\chi = \chi' - i\chi''$$

$$= 1 - F\frac{i\omega\tau_S}{1+i\omega\tau_S} + F\frac{i\omega\tau_S}{(1+i\omega\tau_S)^2}\frac{1}{L}\left[-1+\frac{3}{PL}\left\{Q+\frac{K}{(1+i)\sqrt{PGW\omega\tau_S/2}+1}+\frac{1}{-1+\sqrt{PL}\coth(\sqrt{PL})}\right\}^{-1}\right] \quad \text{Eq. S3}$$

$$L = 1 + i\omega\tau_S\frac{1}{C} - \frac{1}{1+i\omega\tau_S}$$

C, *G*, *P*, *Q*, *W* are dimensionless parameters as summarized in Figure S25. χ' and χ'' are normalized real and imaginary parts of ac magnetic susceptibilities, respectively, ω is an angular frequency ($\omega = 2\pi\nu$), *F* is an adiabatic susceptibility (χ' at high ω limit) and τ_S is the spin-lattice relaxation time. C_{mag}, C_{lat} and C_{bath} are the heat capacities of the spin system, lattice and thermal bath, respectively, r_s is the diameter of sample crystal, α is the heat conduction coefficient between the spin and lattice system, and λ_{lat} and λ_{bath} are heat conduction coefficients for the lattice and thermal bath, respectively. R_K is the heat resistivity between lattice and thermal bath. Figure S26 shows the real and imaginary parts of the ac magnetic susceptibilities determined using Eq. S3 with different values of *M* and *P*. *M* and *P* values, which depend on the concentration of the spin source and the magnetic field, respectively, change the single peak in χ'' vs ν plots into broad and dual ones. In addition, the shapes of the modulated curves are similar to those obtained using experimental ac magnetic susceptibilities.

For fitting the experimental ac magnetic susceptibilities, we normalized χ_M' and χ_M'' to χ_M' value at 1 Hz. The *Q* value (or R_K value) which represents the boundary resistance between the lattice and thermal bath was set to zero to avoid the over parametrization. Fitting the normalized ac magnetic susceptibilities for **GdGd*** afforded the optimized parameters summarized in Figure S28. The field independent parameter *W* is 1.07. The increase in the *C* and *P* values and the decrease in the *G* values with an increase in the dc magnetic strength, as seen in Figure S28, are reasonable because the application of a dc field increases the C_{mag} and α values.

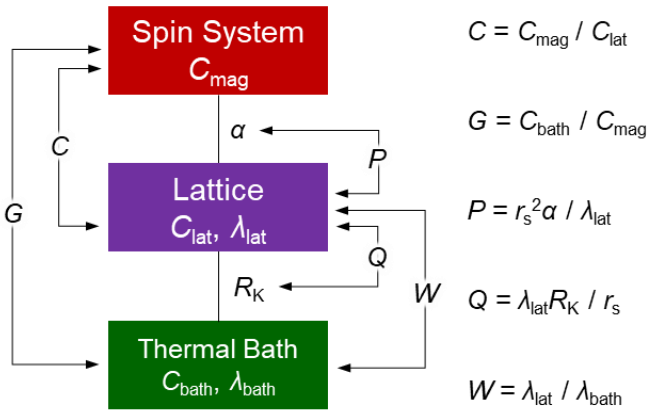

Figure S27. Schematic model of heat transport among the spin system, lattice and thermal bath.[4]

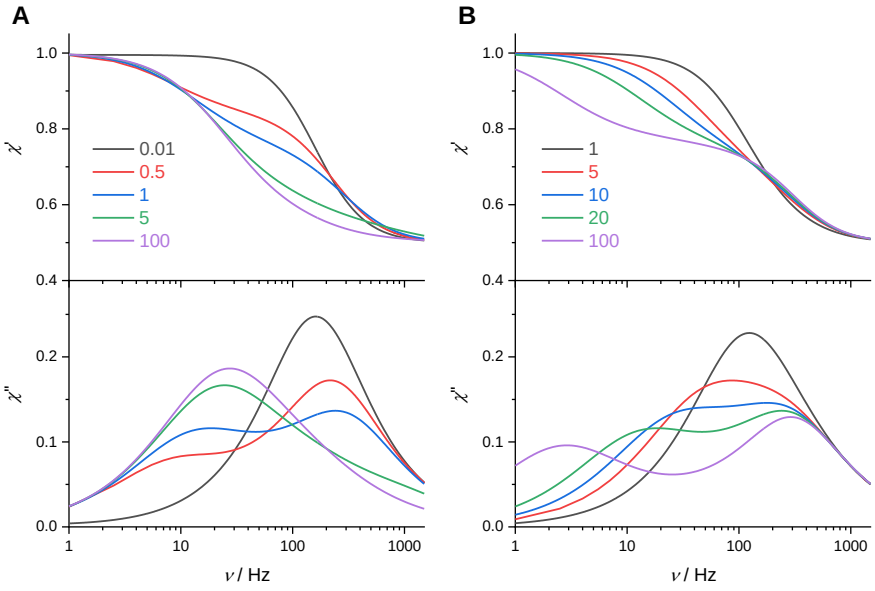

Figure S28. AC magnetic susceptibilities simulated using Eq. S3. A) *C* dependences when *P* = 20, *Q* = 0, *G* = 0.5 and *W* = 1. B) *P* dependences when *C* = 1, *Q* = 0, *G* = 0.5 and *W* = 1.

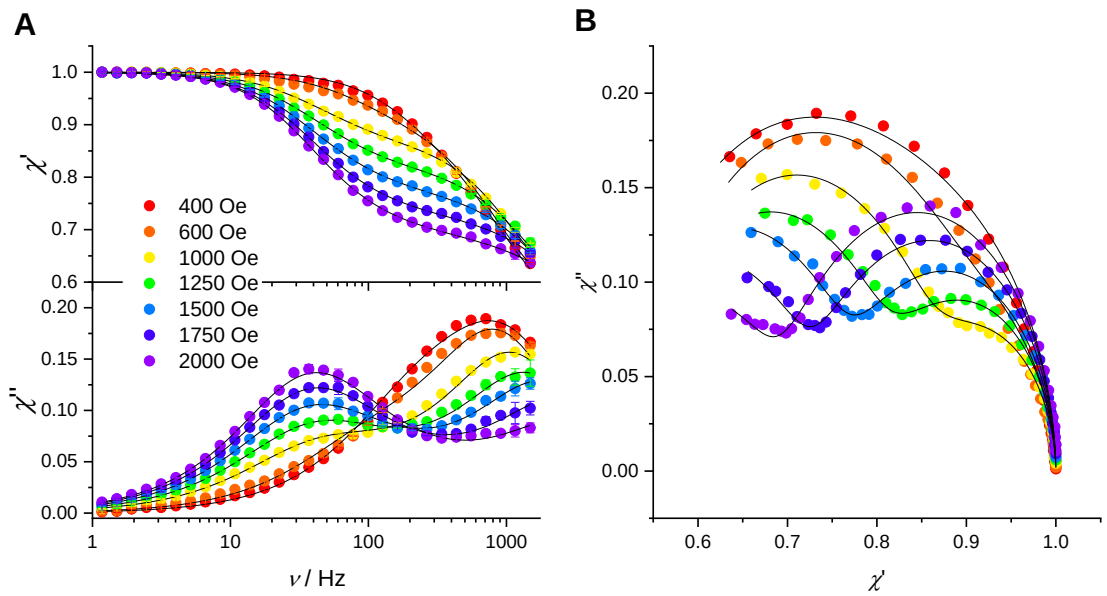

Figure S29. Simulated ac magnetic susceptibilities of **GdGd*** at 1.85 K using Eq. S3. χ_M' and χ_M'' were normalized by χ_M' at 1 Hz.

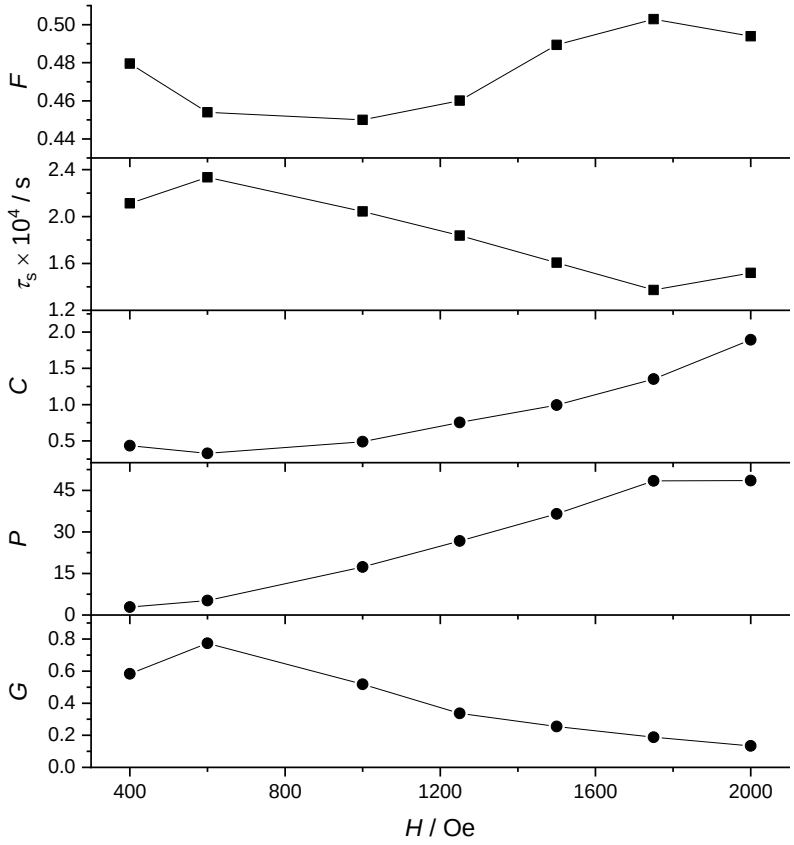

Figure S30. Optimized parameters obtained by fitting the data in Figure S27. *W* value was fixed to 1.07 over the entire field range.

[1] F. Aquilante, J. Autschbach, R. K. Carlson, L. F. Chibotaru, M. G. Delcey, L. De Vico, I. Fdez. Galván, N. Ferré, L. M. Frutos, L. Gagliardi, M. Garavelli, A. Giussani, C. E. Hoyer, G. Li Manni, H. Lischka, D. Ma, P. Å. Malmqvist, T. Müller, A. Nenov, M. Olivucci, T. B. Pedersen, D. Peng, F. Plasser, B. Pritchard, M. Reiher, I. Rivalta, I. Schapiro, J. Segarra-Martí, M. Stenrup, D. G. Truhlar, L. Ungur, A. Valentini, S. Vancoillie, V. Veryazov, V. P. Vysotskiy, O. Weingart, F. Zapata and R. Lindh, *J. Comput. Chem.* **2016**, *37*, 506-541.

[2] L. F. Chibotaru and L. Ungur, *J. Chem. Phys.* **2012**, *137*, 064112.

[3] L. Ungur and L. F. Chibotaru, *Phys. Chem. Chem. Phys.* **2011**, *13*, 20086-20090.

[4] J. Flokstra, G. J. Gerritsma, G. A. Hartemink and L. C. Van Der Marel, *Physica* **1974**, *77*, 99-120.

[5] T. P. Valkering and L. C. Van Der Marel, *Physica* **1970**, *47*, 412-424.